

# Characterization and Control of Nacelle Inlet Flow in Crosswind

Derek A. Nichols<sup>1</sup>, Bojan Vukasinovic<sup>2</sup>, and Ari Glezer<sup>3</sup>  
*Georgia Institute of Technology, Atlanta, GA 30332-0405*

Matthew DeFore, Bradley Rafferty, and Francisco D. Palacios  
*The Boeing Company*

## Abstract

The flow within an inlet of an engine nacelle model is investigated experimentally in the presence of crosswind with specific emphasis on separation over the windward inlet lip. The inlet flow is characterized using arrays of surface static pressure ports and radial total pressure rakes, surface oil-flow visualization, and limited particle image velocimetry. The evolution of the flow topology over the windward lip surface is characterized over a range of crosswind speeds and inlet Mach numbers up to 35 knots and 0.8, respectively. It is shown that the presence of sufficiently high crosswind relative to the inlet speed leads to the formation of a three-dimensional separation domain on the lip's inner surface. The separation domain has an azimuthal, horseshoe-like boundary with its tip near the windward edge – nominally  $0.035D$  downstream of the lip's apex. For a given inlet speed, the azimuthal position of the separation domain is affected by the inclination of the nacelle's inlet plane and the magnitude of the crosswind. As the crosswind speed increases, secondary interacting azimuthal separation cells whose topology resembles the main separation domain are triggered. The present investigation also demonstrates the utility of flow control, specifically a method of passively bleeding air between the outer and inner surfaces of the nacelle for mitigation of the separation. Bleed control leads to reduction in cross stream total pressure deficit and concomitantly to a 3% increase in the inlet's mass flow rate (at a fixed operating point) at crosswind speeds of 30 to 35 knots.

## Nomenclature

$D$	= inlet throat diameter	$p_o$	= total pressure
$\dot{m}$	= mass flow rate	$r$	= radial coordinate
$\dot{m}_c$	= mass flow rate at choking	$U_o$	= crosswind speed
$p$	= static pressure	$\alpha$	= crosswind angle of attack
$p_a$	= atmospheric pressure	$\theta$	= azimuthal coordinate
$P_B$	= blower power	$\zeta$	= mean vorticity

---

<sup>1</sup> Graduate Research Assistant, AIAA Member.

<sup>2</sup> Research Engineer, AIAA Member.

<sup>3</sup> Professor, AIAA Fellow.

## I. Background

Aircraft engine nacelles encounter a range of disparate operating stages including ground taxi, takeoff, climb, cruise, descent, and landing. Although the nacelle inlet is normally optimized for cruise, its design is often compromised for the other operational stages of the flight. Consequently, selecting the aerodynamic design which is best suited for all aspects of the flight is extremely difficult and must take all stages of operation into consideration.

The performance of aircraft engines close to the ground (taxi, takeoff, and landing) can be strongly impacted by the presence of the ground plane and by crosswind that can significantly alter the air intake at the inlet (Trapp et al., 2006). The presence of a crosswind can lead to the formation of a fuselage vortex, inlet flow separation, and, when coupled with ground effect, the formation of a ground vortex that may cause ingestion of debris into the engine (Colehour and Farquhar, 1971, Trapp and Girardi, 2012).

Of particular note is inlet flow separation that can occur in the presence of a crosswind during low speed movements or during climb at steep angles (Savelyev, et al., 2014, Maji et al., 2016). The formation of a highly unsteady separation bubble on the windward edge can produce streamwise vortices and lead to interactions with the fan blades which can cause blade damage and even compressor stall (Übelacker and Kähler, 2016, Radespiel et al. 2016). Furthermore, the separation bubble also decreases the effective cross-sectional area of the inlet and hence the mass flow rate through the engine for a fixed engine pressure ratio (Übelacker et al., 2014). Earlier investigations have also demonstrated that, because of separation hysteresis with varying intake speed, it is especially challenging to force the flow to reattach to the surface (Hall and Hynes, 2006, Colin et al., 2007). Wakelam et al. (2012a, 2012b) conducted low- and high-speed tests on a nacelle cylindrical sector whose inlet was designed to emulate crosswind flow. In this experimental setup, they explored passive boundary layer trips and active vortex-generating jets for mitigation of flow separation at the lip. These authors reported that mitigation of separation within the three-dimensional sector flow led to reduction in total pressure distortion.

This paper focuses on wind tunnel studies of fundamental aspects of flow separation on the surface of the inlet section of a typical commercial airplane nacelle model as a result of crosswind normal to the inlet axis ( $\alpha = 90^\circ$ ). Important emphases of the present investigations are the roles of the independently controlled crosswind speed and nacelle flow rate in the onset and evolution of the separation. The present investigations also demonstrate the utility of flow control based on passive air bleed between the windward outer and inner surfaces of the nacelle for mitigation of the adverse effects of the separation and may enable strategies for utilization of advanced, more efficient nacelle configurations.

## II. Experimental Setup and Flow Diagnostics

The experiments are conducted in a test facility that was recently designed and constructed by Boeing and Georgia Tech for investigations of the physics of nacelle/cross flow interactions and control of their evolution using fluidic actuation. The facility at Georgia Tech comprises two

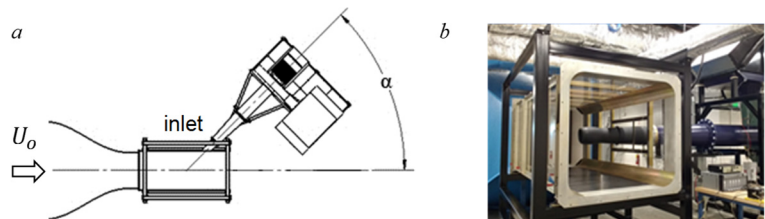


**Figure 1.** Inlet test facility having adjustable inlet angle  $\alpha$ , relative to the crosswind  $U_o$  (a) and a picture of the installed inlet in the crosswind test section.

primary components: a model nacelle assembly and a cross flow wind tunnel (Figure 1). The flow in each component is independently varied, and the position and orientation of the nacelle within the tunnel's test section is variable.

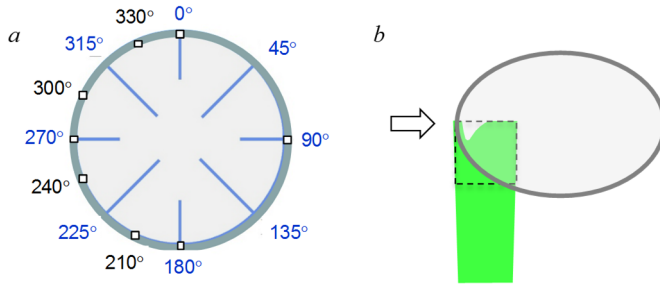


**Figure 2.** Total pressure rake and static port ( $\square$ ) azimuthal orientation (a) and the dashed horizontal PIV field of view (b).

The nacelle model, which can be used to test a broad range of inlet section configurations, is mounted on a flow duct that is driven in suction by a dedicated, computer-controlled blower. The nacelle model, which has a throat inlet diameter  $D$ , is attached to a diffuser followed by a long straight duct segment upstream of the blower's inlet. The duct is equipped with a probe for mass flow rate measurements placed between two flow

straighteners both upstream and downstream. The blower exhaust air is driven into the room through two chilled water heat exchangers so that the ambient air temperature in the room is maintained at a prescribed level to within  $1^\circ\text{C}$ . The nacelle-duct assembly and the blower are supported on a movable frame with casters that enables angular,  $\alpha$ , and axial adjustability about a pivot at the center of the cross flow test section, thereby allowing for adjustment of the nacelle's centerline relative to the crosswind and of the protrusion of the nacelle's inlet into the test section.

The cross flow is generated by an open-return, low-speed wind tunnel having a contraction ratio of 10:1 and is driven by a computer-controlled axial blower. The tunnel's square test section (107 cm on the side) is optically transparent from three sides to enable measurements of the flow field about the nacelle's inlet using particle image velocimetry (PIV) and flow visualization. The uniformity of the air speed within the test section was verified using velocity measurements at various locations of its exit plane.

The nacelle inlet flow is characterized using eight radial rakes of total pressure probes that are distributed azimuthally at  $45^\circ$  increments around the perimeter just upstream of the duct's throat. The number of ports alternates between 10 and 8 in long and short segments as shown schematically in Figure 2a (there are also static pressure ports at the surface next to each rake). In addition, the nacelle inlet is also equipped with 8 streamwise rows of static pressure ports along the nacelle's inlet surface that are marked by square symbols in Figure 2a. The pressure distributions are measured using a dedicated 96-channel pressure scanner (uncertainty better than 1%).

Detailed flow features on the inner surface of the inlet are explored using oil-flow visualization. Oil is placed on the windward side of the nacelle at multiple axial positions between the lip and the total pressure rakes. The inlet flow is also characterized using planar particle image velocimetry (PIV) using a *LaVision* system. Figure 2b illustrates an example of a PIV field of view where the laser sheet intersects the windward lip of the nacelle and the field of view is marked by a dashed rectangle. The CMOS camera ( $2,560 \times 2,160$  pixels) is mounted on a traverse above the test section and is angled to capture a segment of the flow into the inlet.

### III. Inlet Base Flow in Absence of Crosswind

The variation of the mass flow rate through the nacelle ( $\dot{m}$ ) with blower suction was characterized by varying the blower power  $P_B$  (where the maximum blower power is  $P_{B,\max}$ ). The mass flow rate

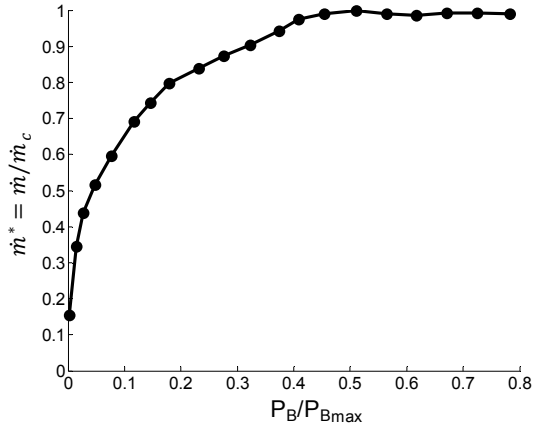


**Figure 3.** Inlet mass flow rate  $\dot{m}^*$  with increasing blower power, in the absence of crosswind.

were used to trip the flow over the inlet lip. Similar tape was used to cover the static pressure ports during the surface oil visualization. Oil flow visualization images of the corresponding flow field about the leading inlet lip are shown in Figures 4a and 4b respectively for  $\dot{m}^* = \dot{m}/\dot{m}_c = 0.99$ . The visualization over the windward azimuthal span ( $180^\circ < \theta < 360^\circ$ ) indicates that the flow turns smoothly and is nearly-uniformly drawn into the inlet – as would be expected in the absence of the crosswind. For reference, the azimuthal positions of the visible total pressure rakes are labeled on the image. This topological feature is supported by PIV measurements in the central horizontal plane  $\theta = 270^\circ$ , as shown in Figure 4b by a color raster plot of the azimuthal vorticity superposed with mean velocity vectors (the image also includes the inlet surface for reference). These data also demonstrate that the surface boundary layer thickens as the inlet flow turns and accelerates around the lip, and that the boundary layer thins as the flow accelerates into the inlet while the core flow aligns with the inlet axis.

Radial distributions of normalized total pressure  $p^* = (p_o - p_a)/p_a$  at the eight azimuthal rake positions (cf. Figure 2) measured for four inlet mass flow rates ( $\dot{m}^* = 0.78, 0.86, 0.98$ , and  $0.99$ ) in the absence of crosswind, are shown in Figure 5. Within the resolution of the measurements, these distributions exhibit no evidence of separation due to flow turning around the nacelle lip and little variation for the different mass flow rates within the core flow. Furthermore, as expected, the total pressure deficit is only measured in the near-wall region due to the boundary layer and increases with the inlet mass flow rate. Overall, the total pressure

through the present nacelle configuration normalized by the choked (or critical) mass flow rate  $\dot{m}_c$  is shown in Figure 3. These data show that following an initial sharp increase,  $\dot{m}$  tapers with increasing blower power until it asymptotes to  $\dot{m}_c$  at just over half of the maximum available blower power and remains unchanged thereafter. Consequently, the facility is well equipped to achieve the maximum possible  $\dot{m}$  through this nacelle model.

An illustration of the flow drawn into the inlet in the absence of the crosswind is shown in Figure 4. As shown in the figure, short strips of tape (approximately  $0.074D$  long,  $4.6$  thousands thick)

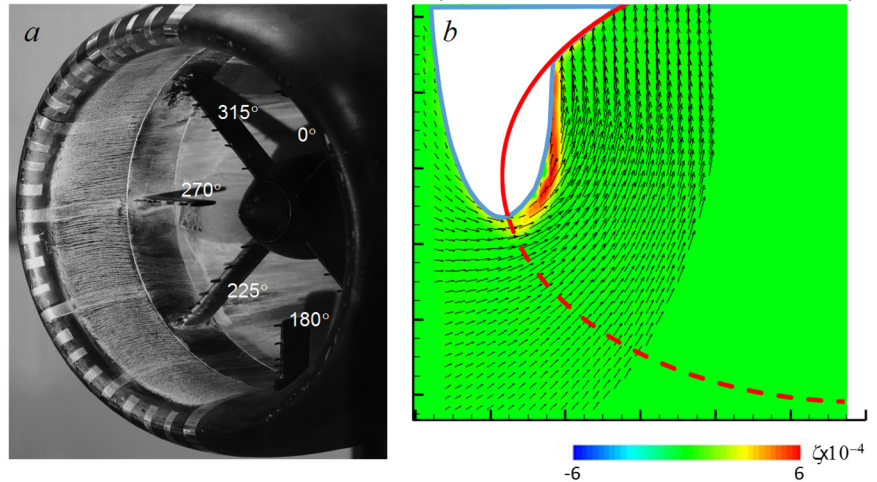


**Figure 4.** Surface oil-flow visualization about the nacelle lip (a) and a raster plot of the mean vorticity  $\zeta$  with overlaid mean velocity vector field (b) for the inlet mass flow rate  $\dot{m}^* = 0.99$  and no crosswind. Schematics of inlet surface are shown for reference.

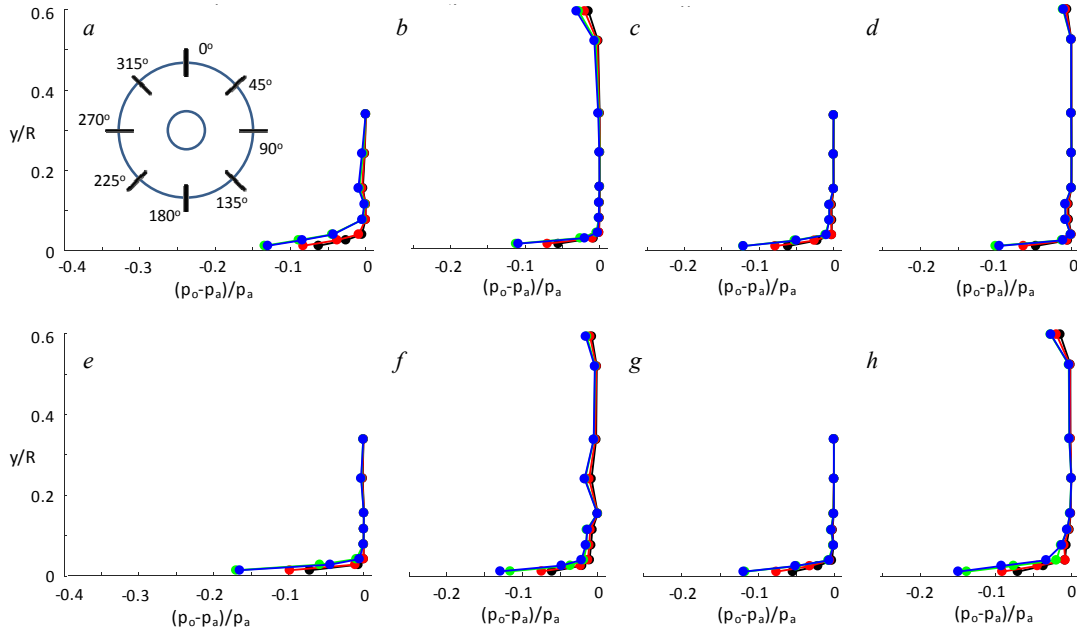


**Figure 5.** Total pressure profiles at eight azimuthal orientations  $\theta = 0^\circ$  (a),  $45^\circ$  (b),  $90^\circ$  (c),  $135^\circ$  (d),  $180^\circ$  (e),  $225^\circ$  (f),  $270^\circ$  (g), and  $315^\circ$  (h) and for four mass flow rates  $\dot{m}^* = 0.78$  (●),  $0.86$  (●),  $0.98$  (●), and  $0.99$  (●).

distributions suggest that, in the absence of crosswind, the inflow is rather smooth with minimal losses.

#### IV. The Effects of Crosswind

The presence of crosswind exacerbates the inlet flow significantly and can lead to separation on the windward side of the inner surface. Oil visualization images of the complex topology of the ensuing flow on an azimuthal segment of the inlet inner surface at a fixed crosswind speed of 35 knots and four inlet mass flow rates  $\dot{m}^* = 0.74, 0.79, 0.94$ , and  $0.98$  are shown in Figure 6. In addition to separation, which is observed for all cases, the oil-flow traces clearly indicate the growing complexity of the flow topology with the increasing  $\dot{m}^*$ . The simplest separation topology occurs at  $\dot{m}^* = 0.74$  (Figure 6a), where a clear separation domain is marked by a horseshoe-like boundary whose narrow leading edge is centered at about  $\theta = 235^\circ$  – well below the horizontal center plane. As the separation pattern spreads azimuthally in the downstream direction, it approximately covers the domain  $205^\circ < \theta < 265^\circ$  just upstream from the total pressure rakes. Besides this main flow separation feature, the flow drawn into the inlet exhibits clear angularity on either side of the separated domain. The angularity of the inlet flow below  $\theta = 235^\circ$  gradually relaxes, such that the flow between  $\theta = 180^\circ$  and about  $205^\circ$  is drawn axially into the inlet as it would in the absence of the cross flow. The incoming flow angularity is even more pronounced above the separation domain. A strong curving outside the separation boundary is seen up to about  $\theta = 315^\circ$ , with evidence of a possible circulating cell on the outer upper boundary centered at about  $\theta = 265^\circ$ . At the lower- and upper-most azimuthal extents, the flow angularity relaxes, and the flow is drawn axially into the inlet over the ranges  $180^\circ < \theta < 210^\circ$  and  $330^\circ < \theta < 360^\circ$ . As the inlet mass flow rate is increased to  $\dot{m}^* = 0.79$  (Figure 6b), no significant changes in the topology are observed, although most of the features become better defined in the oil traces. First, the leading-edge flow separation somewhat widens and slightly shifts upward azimuthally, now centered at about  $\theta = 240^\circ$ . Second, the circulating cell on the upper boundary of the separated

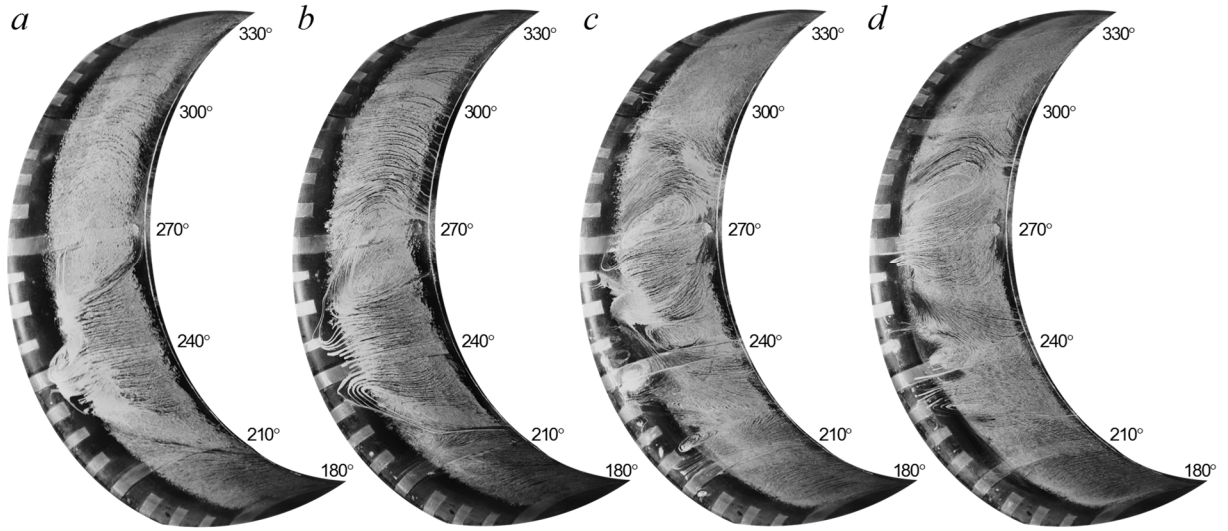


**Figure 6.** Surface oil visualization with  $U_o = 35$  knots cross flow at  $\dot{m}^* = 0.74$  (a),  $0.79$  (b),  $0.94$  (c), and  $0.98$  (d).

region is fully traced, having a focus at about  $\theta = 260^\circ$ . Furthermore, the lower boundary of the separated region depicts an elongated turning line of the flow. Neither of these features is clearly seen in Figure 6a, which might also be attributed to the insufficient shear to oil viscosity ratio in that section of the surface. It is interesting that the overall azimuthal spread of the separated domain remains approximately unchanged in front of the total pressure rakes but is azimuthally offset to  $210^\circ < \theta < 270^\circ$ . Although the lower inlet flow straightens into the inlet at higher azimuthal angles, when compared to the lowest mass flow rate (see the lesser angularity of the lower separation boundary in Figure 6b compared to Figure 6a), there is an additional small irregular flow pattern just downstream of the turning lip at  $\theta = 220^\circ$ . It is also notable that the angularity of the upper flow outside of the separated region somewhat weakens with the increase in  $\dot{m}^*$ , although its relaxation to axial inlet flow does not seem to differ much from the lowest flow rate case (i.e., the axial inlet flow becomes virtually uninterrupted by the crosswind within  $330^\circ < \theta < 360^\circ$ ). The flow topology becomes more complex once the flow rate increases to  $\dot{m}^* = 0.94$  (Figure 6c), primarily over the lower half of the visualized azimuthal domain. The trend of the upward azimuthal migration of the main separation segment continues in this realization as well, such that the upstream initial separation is centered at about  $\theta = 240^\circ$ ; however, the azimuthal extent of this domain is diminished, while it still exhibits an upper circulating cell, which has a focus located at about  $\theta = 275^\circ$ . The overall separation extent upstream of the total pressure rakes is reduced to  $250^\circ < \theta < 275^\circ$ . A major difference relative to lower flow rates is the appearance of multiple small circulating cells that develop on the lower surface, below the lower boundary of the main separated region. The first cell is nested right next to the lower main boundary, at  $\theta = 245^\circ$ , midway between the inlet lip and the rake. Its circulating motion interacts with the smaller lip cell located just below  $\theta = 240^\circ$ , and their synchronous action drives the flow into the inlet in between these two cells. The third cell, which is also located at the lip (at about  $\theta = 215^\circ$ ), gives a rise to opposing flow angularity from below. Hence, these two opposing flow angularities result in an apparent dividing streamline at about  $\theta = 220^\circ$ . In the remaining surface flow over the lower azimuthal section within  $180^\circ < \theta < 210^\circ$ , the outer flow is drawn axially into the inlet with almost no interference from the crosswind. Significant flow angularity is marked in the azimuthal segment immediately above the upper bound of the main separation region, and the higher angularity extends farther towards



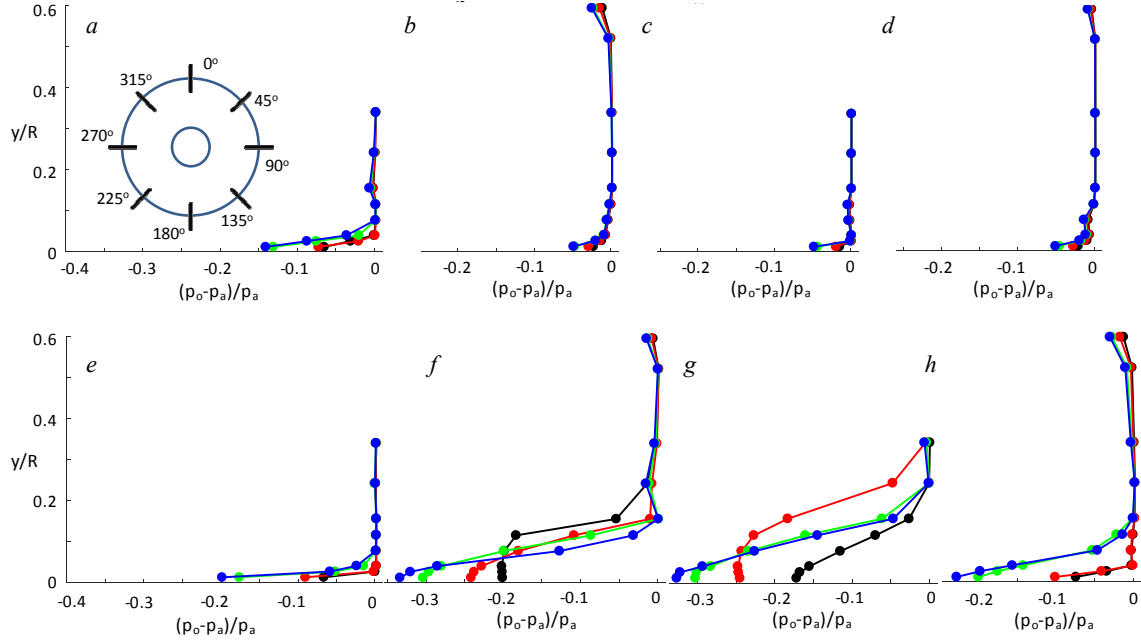


**Figure 7.** Total pressure profiles at eight azimuthal orientations  $\theta = 0^\circ$  (a),  $45^\circ$  (b),  $90^\circ$  (c),  $135^\circ$  (d),  $180^\circ$  (e),  $225^\circ$  (f),  $270^\circ$  (g), and  $315^\circ$  (h) for  $U_o = 35$  knots crosswind and four mass flow rates  $\dot{m}^* = 0.74$  (●),  $0.79$  (●),  $0.94$  (●), and  $0.98$  (●).

higher azimuthal angles and, as in all of the prior cases, the flow becomes axial close to the vertical plane ( $\theta = 360^\circ$ ). Further evolution of the topology pattern is seen in the highest mass flow rate case (Figure 6d). The main separation domain keeps shifting to the higher azimuthal angles, now centered at about  $\theta = 270^\circ$ , while the focal point of the upper-bound circulating cell is at about  $\theta = 285^\circ$ . The overall azimuthal extent of the main separated region is similar to the previous case but shifted upwards to the higher azimuthal angles. The two small circulation cells at the lip that are observed in Figure 6c act in sync at the highest flow rate to form a small compact secondary separation region that mimics the main one. This secondary region is centered at just below  $\theta = 240^\circ$ , and it is bound by the circulating cell above and the extended separation cell along its lower boundary. Still, the axial extent of this secondary separated region is limited, and it does not extend to the streamwise positions of total pressure rakes. Just as the secondary separation domain forms on the lower side of the main separation domain through the evolution of multiple small cells, a small initial cell appears to form at the inlet lip just below the secondary separated region. Further below, towards  $\theta = 180^\circ$ , the flow regains its nominal axial direction as is observed for all other presently considered flow configurations. Similarly, in spite of the additional upward azimuthal change in flow angularity outside of the main separation region, the flow becomes axial near  $\theta = 360^\circ$ .

Radial distributions of the normalized total pressure  $p^* = (p_o - p_a)/p_a$  that correspond to oil images in Figure 6 are shown in Figure 7. These data show that, despite the presence of the crosswind, the three azimuthal stations on the leeward side of the inlet (Figures 7b-d) exhibit a total pressure deficit near the surface that is related to the presence of the boundary layer. Interestingly, these distributions also show slightly reduced near-surface deficits when compared to similar profiles in the absence of the cross flow (Figure 5b-d). In accord with the surface oil flow images, both the top (Figure 7a) and the bottom (Figure 7e) total pressure distributions indicate that the flow about

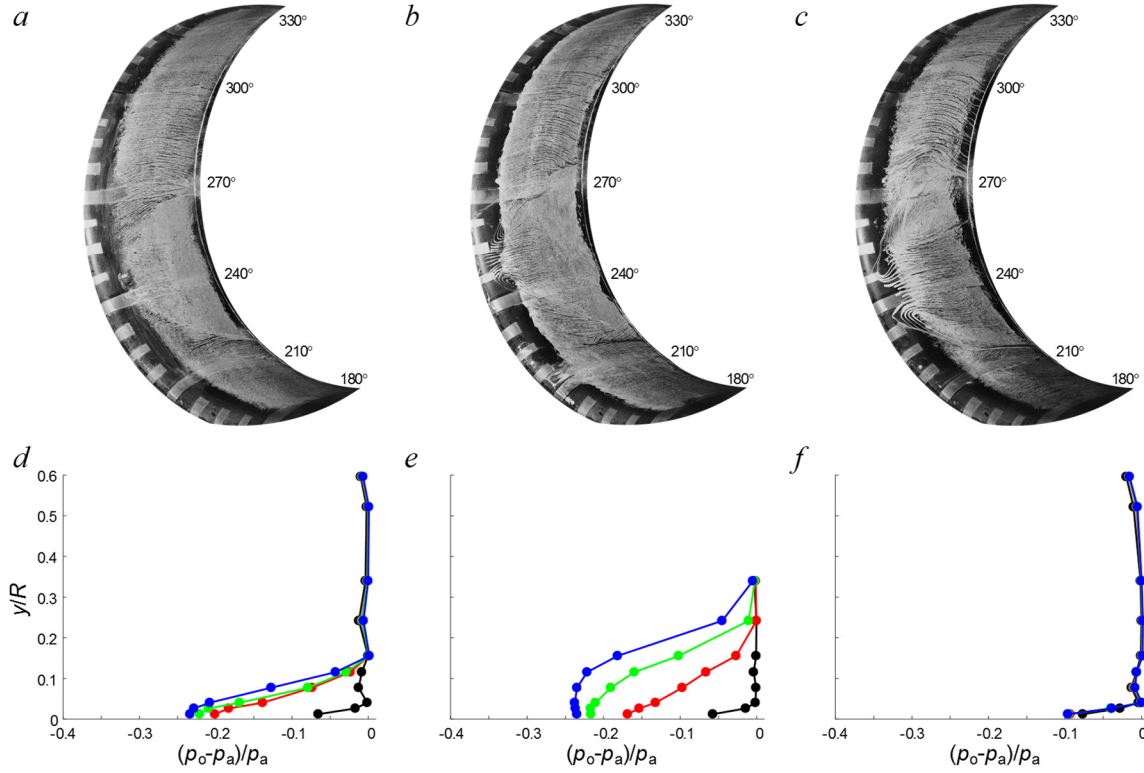


**Figure 8.** Surface oil visualization for fixed mass flow rate at crosswind speeds of 25 (a), 30 (b), and 35 knots (c), and the total pressure profiles corresponding to these cases at three azimuthal locations  $\theta = 225^\circ$  (d),  $270^\circ$  (e),  $315^\circ$  (f) for the crosswind speeds  $U_o = 0$  (●), 25 (●), 30 (●), and 35 (●) knots.

these locations is fairly insensitive to the presence of the crosswind and there is only a slight increase of the total pressure deficit compared to the flow in the absence of the crosswind. As expected from the oil visualization images in Figure 6, the main effects of the crosswind presence are on the windward side, i.e., at the rakes positioned at  $\theta = 225^\circ$ ,  $270^\circ$ , and  $315^\circ$  (Figures 7f-h, respectively). The largest total pressure deficit with the fixed crosswind speed at the changing inlet mass flow rate occurs at  $\theta = 225^\circ$  and  $270^\circ$  (Figures 7f and g, respectively). Both deficits exhibit the same outward radial extent away from the surface at the lowest inlet flow rate, having a more pronounced total pressure loss at  $\theta = 225^\circ$ , while there is an almost negligible increase in deficit at  $\theta = 315^\circ$ . As the mass flow rate is increased to  $\dot{m}^* = 0.79$  (Figure 7h), the dominant radial  $p^*$  deficit is measured at  $\theta = 270^\circ$ , although it is similar to the distribution  $\theta = 225^\circ$  and remains nearly unchanged at the upper section. It is interesting that the distributions of  $p^*$  deficit become very similar at  $\theta = 225^\circ$  and  $270^\circ$  for the two highest inlet mass flow rates. In connection with the oil images in Figure 6, an additional feature compared to the lower mass flow rates is the presence of  $p^*$  deficit at  $\theta = 315^\circ$ , as the main separation region shift towards higher azimuthal angles and flow angularity increases.

Another aspect of the changing flow topology is evident when the crosswind speed is varied at a fixed mass flow rate through the inlet. Three such cases are considered in Figure 8, where the oil flow images equivalent to Figure 6 are shown for  $\dot{m}^* = 0.79$  at crosswind speeds of 25, 30, and 35 knots. Even at the lowest crosswind speed (Figure 8a), there is a clear boundary between the low-speed separated region and the outer flow. The separation horseshoe pattern is centered at  $\theta = 245^\circ$  about the lip and exhibits streamwise broadening within  $220^\circ < \theta < 270^\circ$ . Relatively mild



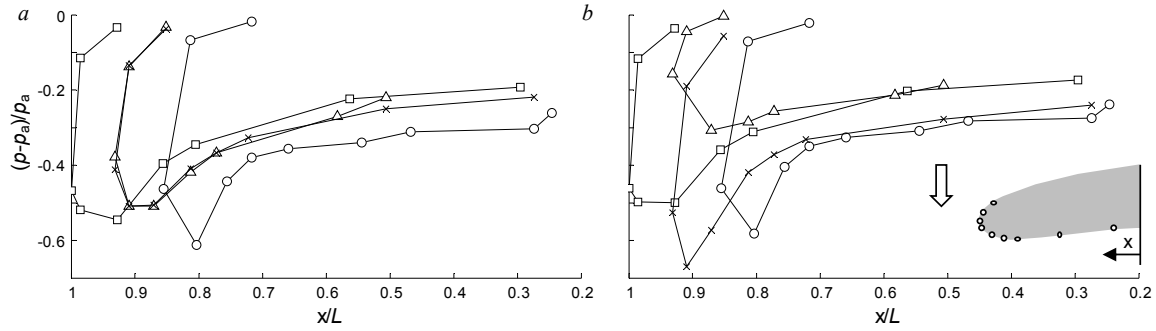


**Figure 9.** Surface static pressure profiles in the absence (a) and presence (b) of crosswind ( $U_o = 30$  knots) at azimuthal locations  $\theta = 0^\circ$  ( $\square$ ),  $90^\circ$  ( $\Delta$ ),  $180^\circ$  ( $\circ$ ), and  $270^\circ$  ( $\times$ ) for the inlet mass flow rate  $\dot{m}^* \approx 0.74$ . Inset schematic illustrates the port arrays.

angularity of the inlet flow is seen on either side of the separated region, which converges to the axial flow over extended azimuthal portions close to the inlet bottom surface, and even more so as the flow approaches the top surface (note that a large upper azimuthal segment starting at about  $\theta = 300^\circ$  and extending up to  $360^\circ$  exhibits almost no interruptions of the nominally axial inlet flow). As the crosswind speed is increased to 30 knots (Figure 8b), the flow separation topology becomes accentuated and develops an azimuthal offset. The initial flow separation about the lip is centered about  $\theta = 250^\circ$ , and the two cell structures become clearly marked along the upper and lower boundaries of the separated domain. Aside from the azimuthal offset, the streamwise azimuthal spread is not significantly altered, but a larger extent of the non-axial flow spreads in either direction compensating for the shift in the separation domain while compared to Figure 8a. The azimuthal extents of the axial flow over the lower and upper segments are about the same and somewhat reduced, respectively. The same separation topology further progresses when the crosswind speed is increased to 35 knots (Figure 8c). However, this time the azimuthal shift of the horseshoe pattern moves downward and is centered at the lip at about  $\theta = 240^\circ$ . Such an azimuthally downward displacement of the separation domain is expected as a result of the effective increase in the ratio between the crosswind speed and the inlet flow, as discussed in connection with the displacement of the separation pattern in Figure 6. As a result of the increase in crosswind speed, the separation domain, the bounding circulation cells, and the flow angularity outside of the separated domain all increase compared to 30 knots crosswind.

The relevant total pressure distributions on the windward side are shown in Figure 8d-f. As expected from the oil flow visualization for all three crosswind speeds, these data show that at  $\theta \approx 315^\circ$  (Figure 8f), there is no additional pressure deficit aside from what is induced by the presence of the boundary-layer. The dominant total pressure deficit is measured at  $\theta = 270^\circ$  (Figure 8e), while there is a peak of a similar magnitude but lower radial extent at  $\theta = 225^\circ$  (Figure 8d). Furthermore, it is seen that the crosswind effect on the total pressure deficit at  $\theta = 225^\circ$  is consistent but weak, as discussed in connection with change in flow topology in that domain. The main changes in the total pressure deficit are observed at the horizontal plane on the windward side (Figure 8e), where there is a progressive increase in both the deficit magnitude and its radial extent with crosswind speed.

The differences between the inlet flows in the absence and presence of lip flow separation due to the crosswind are further analyzed by comparing the characteristic wall static pressure distributions. Figure 9 shows these distributions at  $\theta = 0^\circ$ ,  $90^\circ$ ,  $180^\circ$ , and  $270^\circ$  in the absence (Figure 9a) and presence (Figure 9b) of 30 knots crosswind (cf. Figure 8b). Note that the first two

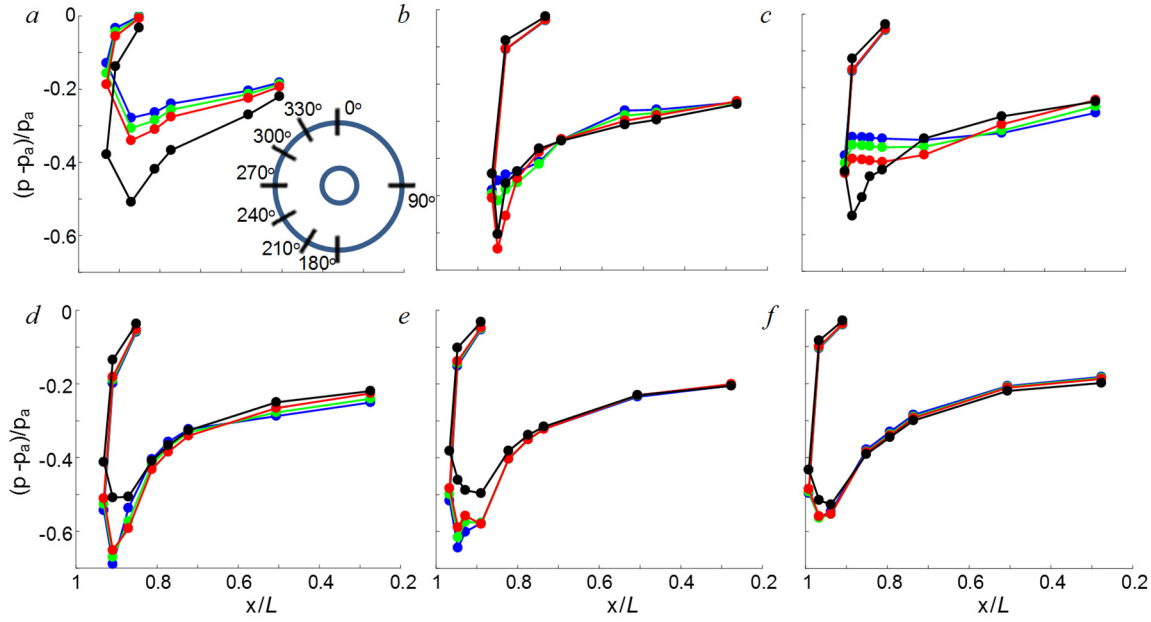


**Figure 10.** Total pressure profiles at six azimuthal orientations  $\theta = 90^\circ$  (a),  $210^\circ$  (b),  $240^\circ$  (c),  $270^\circ$  (d),  $300^\circ$  (e), and  $330^\circ$  (f) for inlet mass flow rate  $\dot{m}^* \approx 0.74$  at crosswind speeds  $U_o = 0$  (●), 25 (●), 30 (●), and 35 knots (●).

static ports are located on the outer lip surface and therefore their axial distance to the reference is lower compared to subsequent ports on the lip apex. Generally, the shape of the profiles is indicative of the flow acceleration over the lip, past which the flow encounters an adverse pressure gradient. It is also noted that, in the absence of a crosswind, the static pressure distributions at  $\theta = 90^\circ$  and  $270^\circ$  are practically identical owing to the symmetry of the inlet about the vertical center plane. All the distributions except at  $\theta = 180^\circ$  reach about the same pressure minimum  $p^* = (p_o - p_a)/p_a \approx -0.55$ , while at  $\theta = 180^\circ$  there is a slightly higher pressure drop indicating a difference between the flow evolution at  $\theta = 0^\circ$  and  $180^\circ$ . This difference results from the acceleration being somewhat higher over the bottom surface due to the inclination of the inlet plane.

The corresponding static pressure distributions in the presence of crosswind are shown in Figure 9b. The least affected are the top and bottom distributions, which do not exhibit any notable differences compared to Figure 9a. Although no flow separation is detected along the static pressure port arrays at  $\theta = 270^\circ$  and  $90^\circ$ , their respective changes compared to the absence of crosswind point to the clear changes in the flow patterns. As the upper circulating separation cell (Figure 8b) drives the flow into the inlet at  $\theta = 270^\circ$ , the corresponding acceleration is manifested by the decrease in static pressure minimum that reaches nearly  $p^* \approx -0.7$  in Figure 9b. Farther downstream, the pressure recovers to similar levels as in Figure 9a, in the absence of crosswind. A significant deceleration of the incoming flow is reflected in the static pressure profile on the leeward side ( $\theta = 90^\circ$ ) where the static pressure about this inlet lip area is elevated relative to the levels in the absence of crosswind (Figure 9a), as the outer flow continuously changes across the inlet and its turning incurs additional losses.

Static pressure distributions for  $\dot{m}^* = 0.74$  at crosswind speeds of 25, 30, and 35 knots are shown in Figure 10, along with the corresponding distributions in the absence of crosswind (the static pressure distributions at  $\theta = 0^\circ$  and  $180^\circ$  are omitted since there is virtually no difference between the presence and absence of crosswind, as indicated by the oil trace images in Figure 8a-c). The

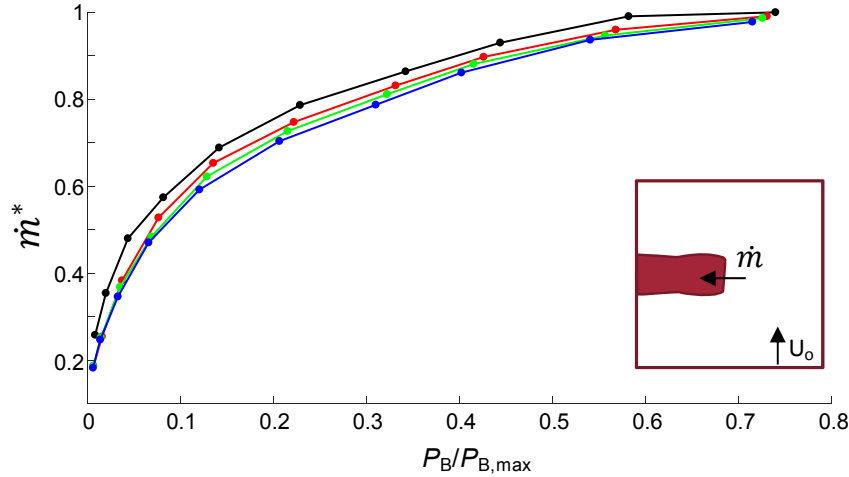


**Figure 11.** Inlet mass flow rate  $\dot{m}^*$  with blower power for the crosswind speed  $U_o = 0$  (●), 25 (●), 30 (●), and 35 (●) knots.

small local circulation cells that form in this region, as clearly captured in Figure 8b. The most dramatic crosswind effect is captured at  $\theta = 240^\circ$  (Figure 10c) which is practically fully encompassed by the separated flow (cf. Figures 8a-c). Clear leveling of the pressure profiles past the turn around the lip indicates a rather abrupt separation regardless of the crosswind speed. In conjunction with the occurrence of separation just below  $\theta = 270^\circ$ , the pressure distributions along the horizontal plane on the windward side (Figure 10d) point to significant flow acceleration about the lip at this area, with a minimum that weakly decreases with the crosswind speed. A rather similar local flow acceleration about the lip is measured at the next azimuthal orientation  $\theta = 300^\circ$  (Figure 10e), but this acceleration almost completely vanishes at  $\theta = 330^\circ$  (Figure 10f) indicating that the upper-most windward side flow is not altered in the presence of the crosswind even when the crosswind induces local separation elsewhere on the windward side of the inlet (as indicated by the oil visualization analysis of Figure 8).

Finally, a global indication of the crosswind effect on the inlet flow is presented in Figure 11 in terms of the variation of the inlet mass flow rate  $\dot{m}^*$  with blower power in the absence and presence (25, 30, and 35 knots) of crosswind. These data indicate similar trends in the drawn mass flow. First, there is a rather sharp increase at low blower power up to about  $\dot{m}^* = 0.5$ , followed by a gradual, smooth diminution of its rate of increase and ultimately asymptotic approach to choking at high blower power where even small increases in mass flow rate require significantly higher power owing to increased losses associated with the appearance of shock waves. In spite of the similar mass flow variations, there is a clear difference between the mass flow rates in the presence and in the absence of crosswind. While in the absence of the crosswind, the flow losses are mostly associated with the friction losses of stagnant flow being smoothly drawn into a high-speed duct, flow losses in the presence of crosswind stem from the turning of the cross flow into the inlet that are exacerbated by complex separation topology (cf., Figures 6 and 8).

## V. Passive Bleed Control

In addition to characterization of the inlet flow in the presence of crosswind, the present investigation also explores the utility of fluidic flow control based on distributed, passive bleed of air between the outer and inner surfaces of the nacelle for mitigation of flow distortion and separation. This approach, which does not require a powered air source, builds on earlier

pressure levels become progressively elevated with increasing crosswind speed (Figure 10a) indicating significant flow deceleration about the horizontal leeward lip. Pressure distributions at  $\theta = 210^\circ$  (Figure 10b) indicate a smooth flow acceleration over the lip at the crosswind of 25 knots, but at 30 and 35 knots, there is a short streamwise leveling just inside the lip which is attributed to the

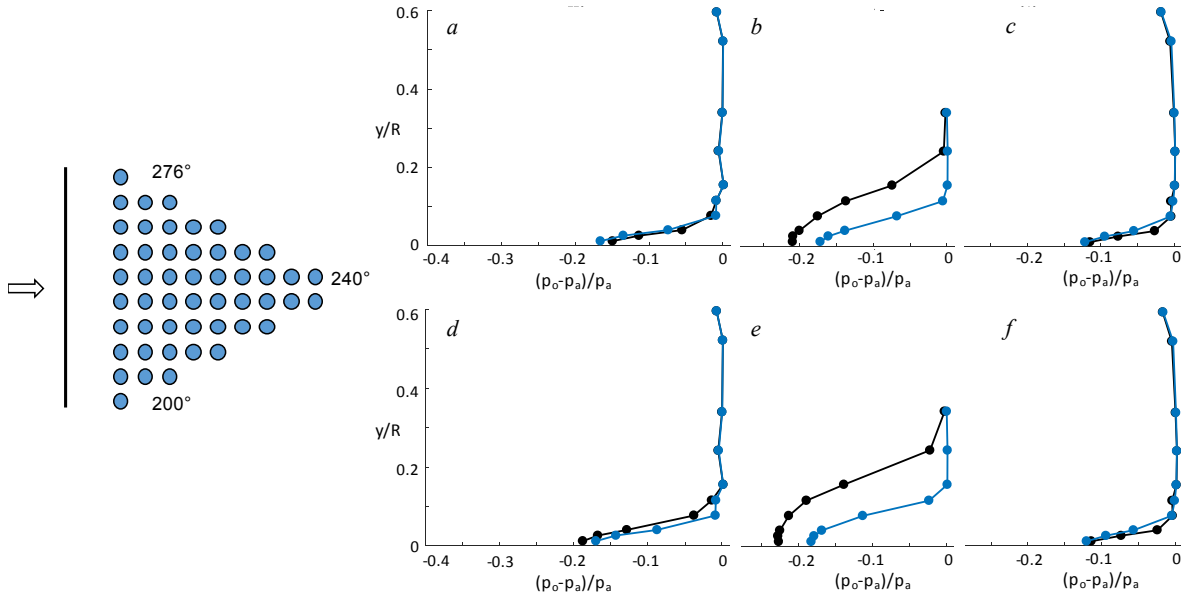


**Figure 12.** Total pressure profiles at three azimuthal orientations  $\theta = 225^\circ$  (a,d),  $270^\circ$  (b,e), and  $315^\circ$  (c,f) at two crosswind speeds  $U_o = 30$  (a-c) and  $35$  (d-f) knots for the uncontrolled ( $\bullet$ ) and controlled ( $\bullet$ ) flow.

investigations at Georgia Tech in which this AFC technology was successfully applied for controlling a range of external and internal flows over aerodynamic surfaces (e.g., Kearney and Glezer, 2013, 2015). Earlier investigations at Georgia Tech (Kearney and Glezer, 2012) demonstrated that the interaction between bleed, that is adjusted by low-power, surface-integrated louver valves, and the cross flow can be tailored to leverage the generation and regulation of vorticity concentrations on or near the surface to alter both attached and separated flows. In the present implementation, the bleed is driven through the nacelle's shell by the inherent pressure differences between the inner and outer windward surfaces and is only regulated by its interaction with the cross flow over the outer and inner shell surfaces. However, it is noted that regulated bleed could enable time-dependent control of inlet flow separation and distortion in varying crosswind speed and direction and inlet mass flow rate during taxi, takeoff, and landing.

In the present study, the bleed ports having characteristic diameter  $d = 0.009D$  are organized in axial arrays at equally spaced azimuthal angles. The centerline of the inlet of each bleed path on the outer shell lies within the same azimuthal ( $r$ - $x$ ) plane through the nacelle's centerline as the outlet port on the surface of the inner shell. The choice of an array of bleed ports is driven by the topology of the separation pattern in the base flow (in the absence of bleed). The effects of bleed control are first investigated using an azimuthal cluster of streamwise arrays that are centered about the azimuthal center of separation at 35 knots ( $\theta = 240^\circ$ , cf. Figure 8c), such that the lengths of adjacent arrays taper off azimuthally in each direction, mimicking the extent of separation as shown schematically in Figure 12. Radial distributions of total pressure in the absence and presence of bleed control are shown for the azimuthal windward rake positions  $\theta = 225^\circ$ ,  $270^\circ$ , and  $315^\circ$  for crosswind speeds of 30 and 35 knots (Figures 12a-c and 12d-f, respectively). Perhaps the most pronounced effect of the bleed actuation is the reduction in total pressure deficit at  $\theta = 270^\circ$  even though the array of bleed ports is centered about  $\theta = 240^\circ$ . Furthermore, an integral measure of the effect of flow control is provided by the change in the inlet mass flow rate (at a given operating point) relative to the uncontrolled flow. Direct measurements of the mass flow rate through the duct indicated that the tested bleed control increased  $\dot{m}$  by about 1.9% and 2.3%

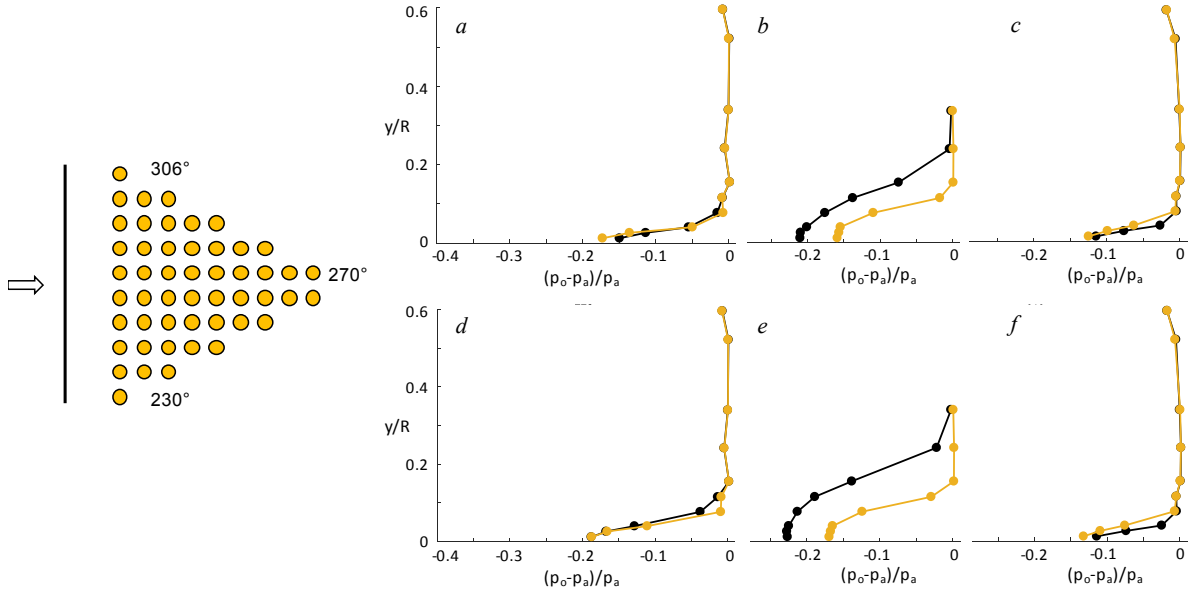


**Figure 13.** Total pressure profiles at three azimuthal orientations  $\theta = 225^\circ$  (a,d),  $270^\circ$  (b,e), and  $315^\circ$  (c,f) at two crosswind speeds  $U_o = 30$  (a-c) and  $35$  (d-f) knots for the uncontrolled (●) and controlled (●) flow.

at 30 and 35 knots crosswind, respectively. This increase in  $\dot{m}$  in the presence of bleed results from reduction in flow losses in addition to the inherently added bleed flow.

As noted earlier, the strongest total pressure deficit (and the total pressure distortion source) is centered at about  $\theta = 270^\circ$  even though the oil visualization indicates that the inlet flow is not separated at this azimuthal angle. Rather, it is affected by the strong circulating cell that bounds the separated domain from above and appears to be nested just upstream of  $\theta = 270^\circ$ . This observation led to a second bleed configuration having a similar azimuthal pattern but centered about  $\theta = 270^\circ$ . This configuration is shown schematically in Figure 14 along with the three radial distributions of total pressure. Again, the effect of the bleed is mostly evidenced about  $\theta = 270^\circ$

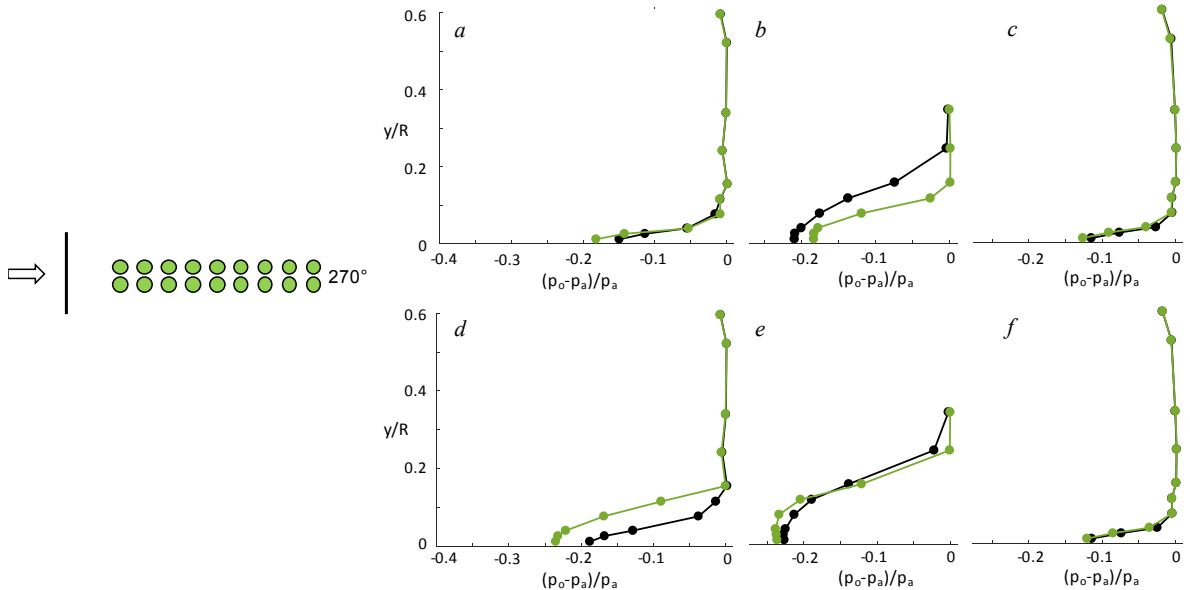


**Figure 14.** Total pressure profiles at three azimuthal orientations  $\theta = 225^\circ$  (a,d),  $270^\circ$  (b,e), and  $315^\circ$  (c,f) at two crosswind speeds  $U_o = 30$  (a-c) and  $35$  (d-f) knots for the uncontrolled (●) and controlled (●) flow.

(Figures 13b and e) and the pressure recovery relative to the uncontrolled flow is similar to Figure 12. However, the increases in inlet mass flow rate are slightly higher: 2.6% and 2.4% for 30 and 35 knots crosswind, respectively.

Given the results in Figures 12 and 13, a third bleed flow control configuration was selected to be a double streamwise row of bleed ports centered about  $\theta = 270^\circ$  as shown schematically in Figure 14 which also includes the resulting total pressure distributions. It is clear that this configuration induces different effects at crosswind speeds of 30 and 35 knots (Figures 14a-c and 14d-f, respectively). While the pressure recovery at 30 knots is comparable to the recovery of the first two bleed configurations, the increase in mass flow rate is increased to 3.6% even though only 36% of the prior bleed ports are used. This indicates that the effect of the actuation can be optimized by dynamically controlling the number and position of active ports with changing flow conditions. This observation is underscored by the fact that when the crosswind speed is increased to 35 knots, the bleed appears to impede the pressure recovery although there is still a slight increase of less than 1% in  $\dot{m}$ . The data in Figure 12 and 13 indicates that fewer streamwise bleed rows could potentially control the flow better at the higher crosswind speed.

## VI. Conclusions

The present experimental study has focused on exploring the topology of the three-dimensional flow and the evolution of complex separation cells over the windward inlet lip of a nacelle in the presence of crosswind. The flow topology is investigated to assist in inlet flow control selection to mitigate adverse effects of separation and distortion. The end objective is to enable integrated nacelle designs that can be dynamically optimized for varying flow conditions during taxi and takeoff/landing without compromising performance in cruise conditions.

The inlet flow in a nacelle model powered by a controlled blower and operating in suction was investigated in a cross-flow wind tunnel. In the absence of crosswind, the outer flow is drawn smoothly into the inlet, and the only deficit in the flow's total pressure is associated with the inlet surface boundary layers. However, the presence of crosswind induces gradual thickening of the deficit region on the windward side of the internal surface of the inlet even prior to the appearance of local separation (at crosswind speed of about 25 knots). The separation domain has a characteristic horseshoe-like streamwise boundary and is azimuthally tilted owing to the inclination of the nacelle's inlet plane, and the degree and direction of the tilt varies with the magnitude of the crosswind. The losses associated with the appearance of flow separation in the presence of crosswind lead to a reduction in the nacelle's mass flow rate compared to the nacelle's flow rate at the same blower power in the absence of crosswind. As the flow separation occurs at high crosswind speeds, the leading edge of the horseshoe separation domain starts just downstream from the apex lip below the central horizontal plane. At lower crosswind speeds, the separation domain begins to shift azimuthally upward but becomes bounded by two additional separation cells at each azimuthal end. Further diminution of the crosswind speed displaces the main separation domain further azimuthally upward and additional secondary separation cells develop and begin to merge and form additional horseshoe separation domains that closely resemble the main domain.

In the present investigation, a novel flow control approach based on scalable, distributed passive air bleed through the nacelle's shell is explored for mitigation of flow separation and distortion. The bleed is driven through configurable ports in the shell by the inherent pressure differences between the inner and outer surfaces and does not require a powered air source. The bleed is



applied through streamwise rows of ports that are equally-spaced azimuthally with the objective of modifying the flow azimuthal asymmetry in the presence of crosswind. The effectiveness of bleed actuation is demonstrated in three bleed configurations that were based on the topology of the separated base flow at a given inlet mass flow rate and the two crosswind speeds of 30 and 35 knots. Bleed configurations that encompass the primary separation domain can lead to diminution of the flow distortion (as measured by radial distributions of the total pressure) and increase the inlet mass flow rate by about 3%. It is also shown that only two streamwise bleed rows (36% of the initial ports) centered at the same azimuthal position as the larger array lead to a similar reduction in distortion and a larger intake mass flow rate. This finding indicates that fewer streamwise dynamically configured bleed ports using integrated surface valves can be tailored to optimally control time-dependent separation and flow distortion at varying crosswind speed and engine power during taxi, takeoff, and landing.

## Acknowledgment

This research has been supported by the Boeing Company and Georgia Tech.

## References

- Colehour, J.L., and Farquhar, B.W., "Inlet Vortex," *J. Aircr.*, vol. 8, no. 1, pp. 39–43, 1971.
- Colin, Y., Aupoix, B., Boussuge, J.F., and Chanez, P., "Numerical Simulation and Analysis of Crosswind Inlet Flows at Low Mach Numbers," *Proc. 8th Int. Symp. Exp. Comput. Aerothermodyn. Intern. Flows*, 2007.
- Hall, C.A., and Hynes, T.P., "Measurements of Intake Separation Hysteresis in a Model Fan and Nacelle Rig," *J. Propuls. Power*, vol. 22, no. 4, pp. 872–879, 2006.
- Kearney, J. M. and Glezer, A., "Aerodynamic Control using Distributed Bleed," *6th Flow Control Conference*, New Orleans, Louisiana, AIAA Paper 2012-3246.
- Kearney, J. M. and Glezer, A., "Aerodynamic Control of a Pitching Airfoil using Distributed Active Bleed," *Proc. 8th International Symposium on Turbulence and Shear Flow Phenomena (TSFP)*, Poitiers, France, 2013.
- Kearney, J. M. and Glezer, A., "Bleed Control of Pitching Airfoil Aerodynamics by Vorticity Flux Modification," *Proc. 9th International Symposium on Turbulence and Shear Flow Phenomena (TSFP)*, Melbourne, Australia, 2015.
- Maji, F., Efraimsson, G., and Reilly, C. J. O., "Potential Improvement of Aerodynamic Performance by Morphing the Nacelle Inlet," *Aerosp. Sci. Technol.*, 54, 122–131, 2016.
- Radespiel, R., François, D.G., Hoppmann, D., Klein, S., and Scholz, P., "Simulation of Wing and Nacelle Stall," *AIAA SciTech*, AIAA Paper 2016-1830.
- Savelyev, A.A., Mikhaylov, S.V., and Zlenko, N.A., "Aerodynamic Inlet Design for Civil Aircraft Nacelle," *Proc. 29th Congr. Int. Counc. Aeronaut. Sci.*, 2014.
- Trapp, L.G., and Girardi, R., "Evaluation of Engine Inlet Vortices Using CFD," *50th AIAA Aerosp. Sci. Meet. Incl. New Horizons Forum Aerosp. Expo.*, AIAA Paper 2012-1200.
- Trapp, L.G., Argentieri, H.G., de Souza, F.J., and Girardi, R.M., "Aspects of Isolated Nacelles Near the Ground During Crosswind Operation," *Proc. ENCIT 2006*, 2006.
- Übelacker, S., Hain, R., and Kähler, C.J., "Flow Investigations in a Stalling Nacelle Inlet Under Disturbed Inflow," *Adv. Simul. Wing Nacelle Stall*, vol. 131, pp. 271-283, 2016.

- Übelacker, S., Hain, R., and Kähler, C.J., “Flow Investigations in a Stalling Nacelle Inlet,” *Proc. 17th Int. Symp. Appl. Laser Tech. to Fluid Mech.*, 2014.
- Wakelam, C.T., Hynes, T.P., Hodson, H.P., Evans, S.W., and Chanez, P., “Separation Control for Aeroengine Intakes, Part 1: Low-Speed Investigation of Control Strategies,” *J. Propuls. Power*, vol. 28, no. 4, pp. 758–765, 2012a.
- Wakelam, C.T., Hynes, T.P., Hodson, H.P., Evans, S.W., and Chanez, P., “Separation Control for Aeroengine Intakes, Part 2: High-Speed Investigations,” *J. Propuls. Power*, vol. 28, no. 4, pp. 766–772, 2012b.